Error analyses of a multistatic meteor radar system to obtain a 3-dimensional spatial resolution distribution

Wei Zhong[1], Xianghui Xue[1,2,3], Wen Yi[1,2], Iain M. Reid[4,5] Tingdi Chen[1,2,3], Xiankang Dou[1,6]

[1]CAS Key Laboratory of Geospace Environment, Department of Geophysics and Planetary Sciences, University of Science and Technology of China, Hefei, China
[2]Mengcheng National Geophysical Observatory, School of Earth and Space Sciences, University of Science and Technology of China, Hefei, China
[3]CAS Center for Excellence in Comparative Planetology, Hefei, China
[4]ATRAD Pty Ltd., Thebarton, South Australia, Australia
[5]School of Physical Sciences, University of Adelaide, Adelaide, South Australia, Australia
[6]Wuhan University, Wuhan, China

Correspondence to: Xianghui Xue (xuexh@ustc.edu.cn)

Abstract: In recent years, the concept of multistatic meteor radar systems has attracted the attention of the atmospheric radar community, focusing on the mesosphere and lower thermosphere (MLT). Recently, there have been some notable experiments using multistatic meteor radar systems. Good spatial resolution is vital for meteor radars because nearly all parameter inversion processes rely on the accurate location of the meteor trail specular point. It is timely then for a careful discussion focussed on the error distribution of multistatic meteor radar systems. In this study, we discuss the measurement errors that affect the spatial resolution and obtain the spatial resolution distribution in 3-dimensional space for the first time. The spatial resolution distribution can both help design a multistatic meteor radar system and improve the performance of existing radar systems. Moreover, the spatial resolution distribution allows the accuracy of retrieved parameters such as the wind fields to be determined.

1 Introduction

The mesosphere and lower thermosphere (MLT) is a transition region from the neutral to the partially ionized atmosphere. It is dominated by the effects of atmospheric waves, including planetary waves, tides and gravity waves. It is also a relatively poorly sampled part of the Earth's atmosphere by ground-based instruments. One widely used approach to sample this region is the meteor radar technique. The ablation of incoming meteors in the MLT region, i.e., ~80 – 110 km, creates layers of metal atoms, which can be observed from the ground by photometry or lidar (Jia et al., 2016; Xue et al., 2013). During meteor ablation, the trails caused by small meteor particles provide a strong atmospheric tracer within the MLT region that can be continuously detected by meteor radar regardless of weather conditions. Consequently, the meteor radar technique has been a powerful tool for studying MLT for decades(Hocking et al., 2001; Holdsworth et al., 2004; Jacobi et al., 2008; Stober et al., 2013; Yi et al., 2018). Most modern meteor radars are monostatic and this has two main limitations in retrieving the complete

wind fields. Firstly, limited meteor rates and relatively low measurement accuracies necessitate that all measurements in the same height range are processed to calculate a "mean" wind. Secondly, classic monostatic radars retrieve wind based on the assumption of a homogenous wind in horizontal and a zero wind in vertical.

The latter conditions can be partly relaxed if the count rates are high and the detections are distributed through a representative range of azimuths. If this is the case, a version of a Velocity Azimuth Display (VAD) analysis can be applied by expanding the zonal and meridional winds using a truncated Taylor expansion (Browning and Wexler, 1968). This is because each valid meteor detection yields a radial velocity in a particular look direction of the radar. The radar is effectively a multi-beam Doppler radar where the "beams" are determined by the meteor detections. If there are enough suitably distributed detections in azimuth in a given observing period, the Taylor expansion approach using cartesian coordinates yields the mean zonal and meridional wind components (u_0, v_0), the horizontal divergence $\left(\frac{\partial u}{\partial x}+\frac{\partial v}{\partial y}\right)$, the stretching $\left(\frac{\partial u}{\partial x}-\frac{\partial v}{\partial y}\right)$ and the shearing $\left(\frac{\partial u}{\partial y}+\frac{\partial v}{\partial x}\right)$ deformations of the wind fields from an analysis of the radial velocities. However, because the radar can only retrieve the wind projection in the radial direction as measured from the radar, the vorticity $\left(\frac{\partial v}{\partial x}-\frac{\partial u}{\partial y}\right)$ of the wind fields is not available. This is common to all monostatic radar systems and a discussion of measurable parameters in the context of multiple fixed beam upper atmosphere Doppler radars is given by (Reid, 1987). Even by relaxing the assumption of a homogeneous wind fields and using the more advanced Volume Velocity Processing (VVP) (Philippe and Corbin, 1979) to retrieve the wind fields, the horizontal gradients of the wind fields cannot be recovered due to the lack of vorticity information. To obtain a better understanding of the spatial variation of the MLT region wind fields, larger area observations (and hence higher meteor count rates) and measurements of the non-homogenous wind fields are needed. An extension of the classic monostatic meteor technique is required to satisfy these needs.

To resolve the limitations outlined above, the concept of multistatic meteor radar systems, such as MMARIA (multi-static and multi-frequency agile radar for investigations of the atmosphere) (Stober and Chau, 2015) and SIMO (single input multiple output) (Spargo et al., 2019), MIMO (multiple input multiple output radar) (Chau et al., 2019) have been designed and implemented (Stober et al., 2018). Multistatic systems can utilize the forward scatter of meteor trails, thus providing another perspective for observing the MLT. Multistatic meteor radar systems have many advantages over classic monostatic meteor radars, such as obtaining higher-order wind fields information and covering wider observation areas. There have been some particularly innovative studies using multistatic meteor radar systems in recent years. For example, by combining MMARIA and the continuous wave multistatic radar technique (Vierinen et al., 2016), Stober and Chau et al. built a 5-station total 7-link multistatic radar network covering an approximately 600 km×600 km region in Germany to retrieve an arbitrary non-homogenous wind fields with a 30 km×30 km horizontal resolution (Stober et al., 2018). Chau et al. used two adjacent classic monostatic specular meteor radars in northern Norway to obtain horizontal divergence and vorticity (Chau et al., 2017). Other approaches, such as coded continuous wave meteor radar (Vierinen et al., 2019) and the compressed sense method in MIMO sparse signal recovery (Urco et al., 2019), are described in the references in these papers.

Analysing spatial resolution in interested areas is a fundamental but difficult topic for meteor radar systems. Meteor radar systems transmit radio waves and then receive radio waves using a cluster of receiver antennas; commonly five antennas as in the Jones et al. configuration (Jones et al., 1998). By analysing the cross correlation of received signals, one can determine the angle of arrivals (AoAs) which includes the zenith angle and azimuth angle denoted as θ and ϕ respectively. By measuring the wave propagation time, one can obtain the range information. Most meteor radar systems rely on specular reflections from meteor trails. Thus, by combining the AoAs and the range information and then using geometric analysis, one can determine the location of meteor trails. Accurately locating the meteor trail specular point (MTSP hereafter) is important since atmospheric parameter retrieval (such as the wind fields or the temperature) depends on the location information of meteor trails. The location accuracy, namely the spatial resolution, determines the reliability of the retrieved parameters. For multistatic meteor radar systems that can relax the assumption of a homogenous horizontal wind fields, the location accuracy becomes a more important issue because the horizontal spatial resolution affects the accuracy of the retrieved horizontal wind fields gradient.

There are some discussions about measuring errors of the meteor radar. For example, a number of studies have discussed AoAs measuring errors (Kang, 2008; Vaudrin et al., 2018; Younger and Reid, 2017). However, those focus on the errors in receiver antennas and seldom discuss the influence of a multistatic configuration on the spatial resolutions. Hocking developed a vertical resolution analysis method in a 2-dimensional baseline vertical section (Hocking, 2018), which simplifies the error propagation process in receiver antennas and put emphasis on how a bistatic meteor radar configuration would affect the vertical resolution in a vertical section. However, Hocking's mothed (HM hereafter) can barely show bistatic configurations' influence on spatial resolution distribution due to ignore the discussion of radial distance measuring error. Moreover, HM is only a demo about vertical resolution in a specific vertical section, not in real three-dimensional space. Hence, for practical purposes, the 3-dimensional spatial distribution of both horizontal resolution and vertical resolution should be considered.

Although multistatic meteor radar systems have developed well experimentally in recent years, the reliability of retrieved atmospheric parameters lacks discussion both for monostatic and multistatic meteor radar. A large part of the reason is that no other measurement technology can provide contrast data for meteor radars in MLT region. On the one hand it proves that meteor radars are irreplaceable in MLT region as a measurement technology; on the other hand, to know the reliability of meteor radars obtained atmospheric parameters and to get better understanding of the dynamic process in MLT region, some quantitative error analyses are necessary and helpful. In this paper, we analyse the multistatic meteor radar resolution distribution in a three-dimensional space for both vertical and horizontal resolution for the first time. And spatial resolution is a prerequisite for evaluating the reliability of retrieved atmospheric parameters, such as wind fields and temperature.

2 Analytical Method

2.1 brief introduction

The HM will be introduced ahead in short to help understand our method. In the HM, measuring errors that affect vertical resolution can be classified into two types (Hocking, 2018) : one is those that caused by the zenith angle measuring error $\delta\theta$ and another is those that caused by the pulse-length effect on vertical resolution. The receiver is a simple antenna pair that is collinear to the baseline (figure 1). HM only calculate vertical resolution in a two-dimensional vertical section which pass though the baseline. The receiver antenna pair is equivalent to one receiver arm in Jones configuration which is comprised of three collinear antennas and is usually in a $2\lambda\backslash2.5\lambda$ configuration. Phase difference of received radio wave between antenna pairs is denoted as $\Delta\Psi$. In meteor radar systems, there ~~are~~ is an acceptable phase difference measuring error (PDME hereafter) $\delta(\Delta\Psi)$. A higher value of $\delta(\Delta\Psi)$ means that more detected signals will be judged as a meteor event meanwhile more misidentifications and bigger errors as well. $\delta(\Delta\Psi)$ is set to approximately 30° (Hocking, 2018; Younger and Reid, 2017) in meteor radar systems. In the HM, the zenith angle measuring error $\delta\theta$ is due to $\delta(\Delta\Psi)$ and $\delta(\Delta\Psi)$ is a constant. Therefore, the error propagation in the receiver is very simple, and $\delta\theta$ is inversely proportional to the cosine of the zenith angle.

Now introduce our analytical method. Our method considers a multistatic system with multiple transmitters and one receiver in 3-dimensional space (figure 2). The receiver is in the Jones configuration, which can be "cross-shaped", "T-shaped" or "L-shaped" in plan view. The five receiver antennas are in the same horizontal plane and constitute two orthogonal antenna arms. To avoid a complex error propagation process in receiver and ~~to~~ place emphasis on multistatic configurations, the PDMEs in the two orthogonal antenna arms ($\delta(\Delta\Psi_1)$ and $\delta(\Delta\Psi_2)$) are constants. Therefore, the AoAs measuring errors (including zenith and azimuth angle measuring errors $\delta\theta$, $\delta\phi$ respectively) can be expressed as a simple function of zenith and azimuth angle. The radial distance is the distance between the MTSP and the receiver, which denoted as R_s. R_s can be determined by combining the AoAs, baseline length $\mathrm{d_i}$, and the radio wave propagating path length R (Stober and Chau, 2015). See figure 4(a), if α, $\mathrm{d_i}$ and R are known, R_s will be calculated easily using Cosine Law as:

$$R_s = \frac{R^2 - d_i^2}{2(R - d_i cos\alpha)} \quad (1)$$

α is the angle between the baseline (i.e. axis-X_i) and the line from the receiver to the MTSP denoted as point A. The multistatic configuration will influence the accuracy of R_s (denoted as δR_s). This is because that α, d and R are determined by the multistatic configuration. We consider the error term δR_s in our method, which is ignored in the HM. δR_s is a function of the AoAs measuring errors ($\delta\theta$ and $\delta\phi$) and the radio wave propagation path length measuring error (denoted as δR). δR is caused by the measuring error of the wave propagation time δt, which is approximately $21\mu s$ (Kang, 2008). Thus, δR can be set as a constant and the default value in our program is $\delta R = c\,\delta t = 6.3km$. It is worth noting that the maximum unambiguous range for pulse meteor radars is determined by the pulse repetition frequency (PRF) (Hocking et al., 2001;

Holdsworth et al., 2004). For multistatic meteor radars utilizing forward scatter, the maximum unambiguous range is c/PRF (where c is the speed of light). For the area where R exceed the maximum unambiguous range, δR is set to positive infinity.

2.2 three kinds of coordinate systems and their transformations

To better depict the multistatic system configuration, three kinds of right-hand coordinate systems (figure 3) need to be established, which are $X_0Y_0Z_0$, $X_iY_iZ_i$ and XYZ. $X_0Y_0Z_0$ is the ENU (east-north-up) coordinate system and axis-X_0, Y_0, Z_0 represent the east, north, up directions respectively. Another two coordinate systems are established to facilitate different error propagations. All types of errors need to be transformed to the ENU coordinate system $X_0Y_0Z_0$ in the end. Coordinate system XYZ is established to depict the spatial configuration of the receiver. XYZ is fixed on the receiver. See figure 3, the coordinate origin of XYZ is on the receiver. Axis-Z is collinear with the antenna boresight and perpendicular to the receiver horizontal plane. Axis-X and axis-Y are collinear with the arms of the two orthogonal antenna arrays. AoAs will be represented in XYZ for convenience. See figure 4, it is convenient to analyse the range information in a plane that goes through the baseline and MTSP. Thus, a coordinate system $X_iY_iZ_i$ is established for a transmitter T_i. The coordinate origins of $X_iY_iZ_i$ are all on the receiver. We stipulate that axis-X_i points to transmitter $\boldsymbol{i}$ **(**$\mathrm{T_i}$). Each pair of T_i and the receiver $\mathrm{R_X}$ constitute a radar link, which is referred to as L_i. The range related information for each L_i will be calculated in $X_iY_iZ_i$. Different types of errors need to propagate to and be compared in $X_0Y_0Z_0$ which is convenient for retrieving wind fields.

We stipulate that clockwise rotation satisfies the right-hand corkscrew rule. By rotating clockwise in order of $\psi_x^{\mathrm{X,i}}$, $\psi_y^{Y,\mathrm{i}}$ and $\psi_z^{Z,\mathrm{i}}$ about axis-X, Y and Z, respectively, one can transform XYZ to $X_iY_iZ_i$. It is worth mentioning that $X_iY_iZ_i$ is non-unique because any rotation about axis-X_i can obtain another satisfactory $X_iY_iZ_i$. Hence, $\psi_x^{\mathrm{X,i}}$ can be set to any values. Similarly, by rotating clockwise in order of $\psi_x^{\mathrm{i,0}}$, $\psi_y^{i,0}$ and $\psi_z^{i,0}$ about axis-X, Y and Z, respectively, one can transform $X_iY_iZ_i$ to $\mathrm{X_0}Y_0Z_0$. To realize the coordinate transformation between those three coordinate systems, coordinate rotation matrix $A_R(\psi_x, \psi_y, \psi_z)$ is introduced. Using A_R, one can transform the coordinate point or vector presentation from one coordinate system to another. The details of the coordinate rotation matrix $A_R(\psi_x, \psi_y, \psi_z)$ can be seen in **Appendix (A.1)**.

2.3 two types of measuring errors

The analytical method of the spatial resolution ~~of~~ for each radar link is the same. The difference between those radar links are only the value of the six coordinates rotation angle ($\psi_x^{\mathrm{X,i}}$, $\psi_y^{Y,\mathrm{i}}$ and $\psi_z^{Z,\mathrm{i}}$; $\psi_x^{\mathrm{i,0}}$, $\psi_y^{i,0}$ and $\psi_z^{i,0}$) and baseline distance $\mathrm{d_i}$. The spatial resolution related measurement errors which will cause location errors of MTSP, can be classified into two types: E_1 is caused by measurement errors in the receiver, and E_2 is due to the pulse length. These two errors are mutually independent. Hence, the total error (E_{total}) can be expressed as:

$$\mathrm{E_{total}^2} = \mathrm{E_1^2} + \mathrm{E_2^2} \tag{2}$$

E_1 is related to three indirect measuring errors. They are zenith, azimuth and radial distance measuring errors, denoted as $\delta\theta$, $\delta\phi$ and δR_s respectively. In XYZ, E_1 can be decomposed into three orthogonal error vectors using $\delta\theta$, $\delta\phi$ and δR_s (figure 4(c)). Now we explain it in detail. PDMEs, i.e. $\delta(\Delta\Psi_1)$ and $\delta(\Delta\Psi_2)$, are caused by some practical factors, such as phase calibration mismatch and the fact that specular point is not actually a point but has a few Fresnel zones length. A meteor radar system calculates phase difference of different pair of antennas though cross-correlations and then fit them to get the most likely AoAs. Therefore, the system needs to set a tolerant value of $\delta(\Delta\Psi_1)$ and $\delta(\Delta\Psi_2)$. Different meteor radar systems have different AoAs-fit algorithms and thus different AoAs measuring error distribution. To analyses the spatial resolution for a SIMO meteor radar system as common as possible and to avoid tedious error propagation in receiver, we start error propagation from $\delta(\Delta\Psi_1)$ and $\delta(\Delta\Psi_2)$ and set them as constant. AoAs measuring errors, i.e. $\delta\theta$ and $\delta\phi$ can be expressed as:

$$\delta\theta = \frac{\lambda}{2\pi D_1}\frac{\cos\phi}{\cos\theta}\delta(\Delta\Psi_1) + \frac{\lambda}{2\pi D_2}\frac{\sin\phi}{\cos\theta}\delta(\Delta\Psi_2) \quad (3)$$

$$\delta\phi = \frac{\lambda}{2\pi D_2}\frac{\cos\phi}{\sin\theta}\delta(\Delta\Psi_2) - \frac{\lambda}{2\pi D_1}\frac{\sin\phi}{\sin\theta}\delta(\Delta\Psi_1) \quad (4)$$

λ is the radio wave length. D_1 and D_2 are the length of the two orthogonal antenna arms. θ and ϕ are the zenith angle and the azimuth angle, respectively. The details can be seen in **Appendix (A.2).** It is worth noting that $\delta\theta$ and $\delta\phi$ are not mutually independent. The Expectation value of their product is not identical to zero unless $\frac{E(\delta^2(\Delta\Psi_1))}{D_1^2}$ is equal to $\frac{E(\delta^2(\Delta\Psi_2))}{D_2^2}$.

δR_s can be expressed as a function of δR, $\delta\theta$ and $\delta\phi$ as:

$$\delta R_s = F(\delta R, \delta\theta, \delta\phi) = f_R(\theta,\phi)\delta R + f_\theta(\theta,\phi)\delta\theta + f_\phi(\theta,\phi)\delta\phi \quad (5)$$

$f_R(\theta,\phi)$, $f_\theta(\theta,\phi)$ and $f_\phi(\theta,\phi)$ are the weight functions of δR_s. The details about the weight function and deduction can be found in **Appendix (A.3)**. See figure 4(c), E_1 can be decomposed into three orthogonal error vectors in coordinate XYZ, denoted as $\overrightarrow{\delta R_s}$, $\overrightarrow{R_s\delta\theta}$ and $\overrightarrow{R_s sin\theta\delta\phi}$. These three vectors can be expressed in XYZ as:

$$\overrightarrow{\delta R_s} = \delta R_s(\sin\theta\cos\phi, \sin\theta\sin\phi, \cos\theta)^T \quad (6)$$

$$\overrightarrow{R_s\delta\theta} = R_s\delta\theta(\cos\theta\cos\phi, \cos\theta\sin\phi, -\sin\theta)^T \quad (7)$$

$$\overrightarrow{R_s\sin\theta\delta\phi} = R_s\sin\theta\delta\phi(-\sin\phi, \cos\phi, 0)^T \quad (8)$$

E_2 is related to the radio wave propagating path. A pulse might be reflected anywhere within a pulse length (figure 4(b)). This causes a location error of MTSP, represented as an error vector $\overrightarrow{DA}$. D is the median point of isosceles triangle ΔABC's side BC. The representation of the error vector $\overrightarrow{DA}$ can be solved in $X_iY_iZ_i$ by using geometry relationship as:

$$\overrightarrow{DA} = \left(\frac{(2-a_1-a_2)x_i + d_i(a_2-1)}{2}, \frac{(2-a_1-a_2)y_i}{2}, \frac{(2-a_1-a_2)z_i}{2}\right)^T \quad (9)$$

S is half wave pulse length and $a_1 = \frac{R_s - S}{R_s}$. $a_2 = \frac{R_i - S}{R_i}$. d_i is the baseline length. (x_i, y_i, z_i) is the coordinate value of a MTSP (i.e. point A in figure 4) in $X_iY_iZ_i$. Details can be seen in **Appendix (A4)**

2.4 transform to ENU coordinate

Here, two types of errors in different coordinate systems have been introduced. Now they need to be transformed to ENU coordinates $X_0Y_0Z_0$, which is convenient for comparing between different radar link and analysing wind fields. E_1 related error vectors, which are three orthogonal vectors $\overrightarrow{\delta R_s}$, $\overrightarrow{R_s\delta\theta}$ and $\overrightarrow{R_s sin\theta\delta\phi}$ and represented in XYZ as eq.(6)-(8), need to be transformed from XYZ to $X_0Y_0Z_0$.To project $\overrightarrow{\delta R_s}$, $\overrightarrow{R_s\delta\theta}$ and $\overrightarrow{R_s sin\theta\delta\phi}$ towards axis-X_0, Y_0, Z_0 respectively and reassemble them to form three new error vectors in axis-X_0, Y_0, Z_0. Using coordinate rotation matrix $A_R^{(XYZ, X_0Y_0Z_0)} = A_R(\Psi_x^{i,0}, \Psi_y^{i,0}, \Psi_z^{i,0}) \cdot A_R(\psi_x^{X,i}, \psi_y^{Y,i}, \psi_z^{Z,i})$ and eq.(6)-(8), the unit vectors of those three vectors can be represented in $X_0Y_0Z_0$ as:

$$\begin{pmatrix} X_0'(\delta R_s) & X_0'(\delta\theta) & X_0'(\delta\phi) \\ Y_0'(\delta R_s) & Y_0'(\delta\theta) & Y_0'(\delta\phi) \\ Z_0'(\delta R_s) & Z_0'(\delta\theta) & Z_0'(\delta\phi) \end{pmatrix} = A_R^{(XYZ,\ X_0Y_0Z_0)} \cdot \begin{pmatrix} sin\theta cos\phi & cos\theta cos\phi & -sin\phi \\ sin\theta sin\phi & cos\theta sin\phi & cos\phi \\ cos\theta & -sin\theta & 0 \end{pmatrix} \quad (10)$$

$\left(X_0'(\delta R_s), Y_0'(\delta R_s), Z_0'(\delta R_s)\right)^T$, $\left(X_0'(\delta\theta), Y_0'(\delta\theta), Z_0'(\delta\theta)\right)^T$, $\left(X_0'(\delta\phi), Y_0'(\delta\phi), Z_0'(\delta\phi)\right)^T$ are unit vectors of $\overrightarrow{\delta R_s}$, $\overrightarrow{R_s\delta\theta}$ and $\overrightarrow{R_s sin\theta\delta\phi}$ in $X_0Y_0Z_0$ respectively. The 3×3 matrix in left side of the eq.(10) is denoted as P_{ij} for $i, j = 1,2,3$.

See eq.(6)-(8) and figure 4(c), the length of those three vectors, or error values in other words, are δR_s, $R_s\delta\theta$, $R_s sin\theta\delta\phi$ as the function of $\delta R, \delta\theta, \delta\phi$. In order to reassemble them to new error vectors, transforming $\delta\theta$ and $\delta\phi$ into two independent errors $\delta(\Delta\Psi_1)$ and $\delta(\Delta\Psi_2)$ are needed because $\delta\theta$ and $\delta\phi$ are not independent. Using eq. (3) and (4), one can transform vector $(\delta R\ ,\ \delta\theta\ ,\ \delta\phi)^T$ to three independent measuring errors δR, $\delta(\Delta\Psi_1)$ and $\delta(\Delta\Psi_2)$. And thus $(\delta R_s,\ R_s\delta\theta,\ R_s sin\theta\delta\phi)^T$ can be expressed as:

$$\begin{pmatrix} \delta R_s \\ R_s\delta\theta \\ R_s sin\theta\delta\phi \end{pmatrix} = \begin{pmatrix} f_R(\theta,\phi) & f_\theta(\theta,\phi) & f_\phi(\theta,\phi) \\ 0 & R_s & 0 \\ 0 & 0 & R_s sin\theta \end{pmatrix} \cdot \begin{pmatrix} 1 & 0 & 0 \\ 0 & \frac{\frac{\lambda}{2\pi}}{cos\theta}\frac{cos\phi}{D_1} & \frac{\frac{\lambda}{2\pi}}{cos\theta}\frac{sin\phi}{D_2} \\ 0 & -\frac{\frac{\lambda}{2\pi}sin\phi}{sin\theta D_1} & \frac{\frac{\lambda}{2\pi}cos\phi}{sin\theta D_2} \end{pmatrix} \cdot \begin{pmatrix} \delta R \\ \delta(\Delta\Psi_1) \\ \delta(\Delta\Psi_2) \end{pmatrix} \quad (11)$$

The product of the first and the second term in right side of eq.(11) is a 3×3 matrix, denoted as W_{ij} for $i, j = 1,2,3$. Seen eq.(11), three error valuesδR_s, $R_s\delta\theta$, $R_s sin\theta\delta\phi$ are the linear combinations of three basis $\delta R, \delta(\Delta\Psi_1), \delta(\Delta\Psi_2)$ with their corresponding linear coefficients W_{1j}, W_{2j}, W_{3j}. Those three error values can be projected toward new directions (i.e. axis-X_0, Y_0, Z_0) by using P_{ij}. It worth noting that in a new direction, a same basis's projected linear coefficients from different error values should be used to calculate their sum of squares (SS). And then the square root of SS will be used as a new linear coefficient for that basis in the new direction. For example, in X_0 directions, basis $\delta(\Delta\Psi_1)$'s projected linear coefficients are $X_0'(\delta R_s)W_{12}$, $X_0'(\delta\theta)W_{22}$,$X_0'(\delta\phi)W_{32}$ from $\overrightarrow{\delta R_s}$, $\overrightarrow{R_s\delta\theta}$ and $\overrightarrow{R_s sin\theta\delta\phi}$ respectively. Therefore, the new linear coefficient

for $\delta(\Delta\Psi_1)$ in X_0 direction is $\mathrm{W}_{\mathrm{X}_0'}^{\delta(\Delta\Psi_1)} = \pm\sqrt{(\mathrm{X}_0'(\delta R_s)W_{12})^2 + (\mathrm{X}_0'(\delta\theta)\mathrm{W}_{22})^2 + (\mathrm{X}_0'(\delta\phi)\mathrm{W}_{32})^2}$. Similarly, one can get δR and $\delta(\Delta\Psi_2)$'s new linear coefficients in X_0', denoted as $\mathrm{W}_{\mathrm{X}_0'}^{\delta\mathrm{R}}$ and $\mathrm{W}_{\mathrm{X}_0'}^{\delta(\Delta\Psi_2)}$.Thus true error values in X_0 direction is $\mathrm{W}_{\mathrm{X}_0'}^{\delta\mathrm{R}}\delta R + \mathrm{W}_{\mathrm{X}_0'}^{\delta(\Delta\Psi_1)}\delta(\Delta\Psi_1) + \mathrm{W}_{\mathrm{X}_0'}^{\delta(\Delta\Psi_2)}\delta(\Delta\Psi_2)$. Because $\delta\mathrm{R}, \delta(\Delta\Psi_1), \delta(\Delta\Psi_2)$ are mutually independent, E_1 related mean square error (MSE) values in X_0 direction, denoted as $\delta_{(1)}X_0$, can be expressed as $\delta_{(1)}X_0 = \pm\sqrt{\left(W_{X_0'}^{\delta R}\delta R\right)^2 + \left(W_{X_0'}^{\delta(\Delta\Psi_1)}\delta(\Delta\Psi_1)\right)^2 + \left(W_{X_0'}^{\delta(\Delta\Psi_2)}\delta(\Delta\Psi_2)\right)^2}$.

In short, E_1 related errors in ENU coordinate's three axis directions (denoted as $\delta_{(1)}X_0, \delta_{(1)}Y_0$ *and* $\delta_{(1)}Z_0$) can be expressed in the form of matrix as:

$$\begin{pmatrix}\delta_{(1)}^2X_0\\ \delta_{(1)}^2Y_0\\ \delta_{(1)}^2Z_0\end{pmatrix} = P_{ij}^2 \cdot W_{ij}^2 \cdot \begin{pmatrix}\delta^2R\\ \delta^2(\Delta\Psi_1)\\ \delta^2(\Delta\Psi_2)\end{pmatrix} \tag{12}$$

E_2 related error vector $\overrightarrow{DA}$ needs transformation from $X_iY_iZ_i$ to $X_0Y_0Z_0$. Therefore, E_2 related errors in ENU coordinate's three axis directions (denoted as $\delta_{(2)}X_0, \delta_{(2)}Y_0$ *and* $\delta_{(2)}Z_0$) can be expressed in the form of matrix as:

$$\begin{pmatrix}\delta_{(2)}X_0\\ \delta_{(2)}Y_0\\ \delta_{(2)}Z_0\end{pmatrix} = \pm A_R(\Psi_x^{i,0}, \Psi_y^{i,0}, \Psi_z^{i,0}) \cdot \overrightarrow{\mathrm{DA}} \tag{13}$$

E_1 and E_2 are mutually independent. By using eq.(1), the total MSE values in ENU coordinate's three axis directions (denoted as $\delta_{\mathrm{total}}X_0$, $\delta_{\mathrm{total}}Y_0$ and $\delta_{\mathrm{total}}Z_0$) can be expressed in the form of matrix as:

$$\begin{pmatrix}\delta_{\mathrm{total}}^2X_0\\ \delta_{total}^2Y_0\\ \delta_{total}^2Z_0\end{pmatrix} = \begin{pmatrix}\delta_{(1)}^2X_0\\ \delta_{(1)}^2Y_0\\ \delta_{(1)}^2Z_0\end{pmatrix} + \begin{pmatrix}\delta_{(2)}^2X_0\\ \delta_{(2)}^2Y_0\\ \delta_{(2)}^2Z_0\end{pmatrix} \tag{14}$$

In conclusion, for a radar link L_i and a MTSP represented as $(\mathrm{x}_0, \mathrm{y}_0, \mathrm{z}_0)$ in ENU coordinate system $X_0Y_0Z_0$, as figure 4(a) sketched, the location errors of this point in east, north and up directions ($\pm\delta_{\mathrm{total}}X_0$, $\pm\delta_{\mathrm{total}}Y_0$ and $\pm\delta_{\mathrm{total}}Z_0$) can be calculated as follows: firstly, for a point $(\mathrm{x}_0, \mathrm{y}_0, \mathrm{z}_0)$ in $\mathrm{X}_0'\mathrm{Y}_0'\mathrm{Z}_0'$, using A_R to transform it to $X_iY_iZ_i$ and denoted as $(\mathrm{x_i}, \mathrm{y_i}, \mathrm{z_i})$. Then in $X_iY_iZ_i$ calculate AoAs (θ and ϕ) and range information ($\mathrm{R_s}$ and $\mathrm{R_i}$). Details of AoAs and range calculation can be seen in **Appendix (A.5)**. It's worth noting that AoAs are the angles relative to axis of XYZ. Secondly, in XYZ using AoAs and eq.(3)-(8) to calculate E_1's three orthogonal error vectors as figure 4(c) sketched; in $X_iY_iZ_i$ use range information and eq.(9) to calculate E_2's error vector $\overrightarrow{\mathrm{DA}}$ as figure 4(b) sketched. Thirdly, project E_1's three error vectors to $X_0Y_0Z_0$ by using eq.(10) and use eq.(11)-(12) to reassemble them to calculate E_1 related MSE values in direction of

X_0, Y_0, Z_0; use eq.(13) to transform E_2 error vector from $X_iY_iZ_i$ to $X_0Y_0Z_0$. Finally, use eq. (14) to get the total location errors of a MTSP in (x_0, y_0, z_0). Figure 5(a) describes the process above.

3 Results and Discussion

We wrote a program to study the method above. The program is written in python language and is presented in supplement. To calculate a special configuration of a multistatic radar system, we initially need to set six coordinate transformation angles ($\psi_x^{X,i}$, $\psi_y^{Y,i}$ and $\psi_z^{Z,i}$; $\psi_x^{i,0}$, $\psi_y^{i,0}$ and $\psi_z^{i,0}$) and baseline length (i.e. $\mathbf{d_i}$) for each radar link L_i. For example, $\psi_x^{i,0} = \psi_y^{i,0} = 0$, $\psi_z^{i,0} = 30°$ and $d_i = 250km$ means a transmitter T_i is 250km, 30° east by south of the receiver R_X; Further, $\psi_x^{X,i} = 5°, \psi_y^{Y,i} = 0, \psi_z^{Z,i} = 0$ means one receiver arm (axis-Y) points to east by north 60° with 5° elevation. The interested detection area of multistatic meteor radar is usually from 70km to 110km in height and lager than 300km×300km in horizontal. In our program, this area needs to be divided into a spatial grid for sampling. The default value of the sampling grid length is 1km in height and 5km in meridian and zonal directions. After the settings mentioned above, the program will traverse those sampling grid nodes and calculate the location errors of each nodes as described in figure 5(a). Figure 5(b) describe the parameter settings and traversal calculation process above. For a given setting of radar link L_i, the program will output the squared values of E_1 related, E_2 related and total MSE (E_{total}^2: $\delta_{total}^2 X_0$, $\delta_{total}^2 Y_0$, $\delta_{total}^2 Z_0$; E_1^2: $\delta_{(1)}^2 X_0$, $\delta_{(1)}^2 Y_0$, $\delta_{(1)}^2 Z_0$; E_2^2: $\delta_{(2)}^2 X_0$, $\delta_{(2)}^2 Y_0$, $\delta_{(2)}^2 Z_0$). The location errors can be positive or negative and thus the spatial resolutions are twice the absolute value of location errors. For example, See figure 5(c), for a detected MTSP represented as (x_0, y_0, z_0) in $X_0Y_0Z_0$, if $\delta_{total}^2 X_0$, $\delta_{total}^2 Y_0$, $\delta_{total}^2 Z_0$ equals 25, 16 and 9 km^2 respectively, it means that the actual position of MTSP could occur in an area which is ± 5 km, ± 4 km, ± 3 km around (x_0, y_0, z_0) with equally probability. The zonal, meridian and vertical resolution are 10 km, 8 km and 6 km respectively.

The HM analyses vertical resolution (corresponding to δZ_0 in our paper) only in a 2-dimensional vertical section (corresponding to the X_0Z_0 plane in our paper). To compare with Hocking's work, except $\psi_z^{i,0}$ set to be 180°, other five coordinate transformation angles are all set to zero with **d** is equal to 300 km. The half wave pulse length S is set to 2 km and $\delta(\Delta\Psi_1)$ to 35°. Calculating in only the X_0Y_0 plane should have degraded our method into Hocking's 2-dimensional analysis method, but the settings above doesn't work because Hocking's method ignores δR_s. In fact, Hocking's method considers only E_2 and $\overrightarrow{R_s \delta\theta}$ in the X_0Y_0 plane. Hence, we need to further set $f_R(\theta, \phi)$, $f_\theta(\theta, \phi)$ and $f_\phi(\theta, \phi)$ to be zero. Thus, our method totally degrades into Hocking's method. Hocking's results are shown in the absolute value of vertical location error normalized relative to half wave pulse width, i.e. $|\delta Z_0|/S$. Hereafter, $|E|/S$ is referred to normalized spatial resolutions such as $\delta_{(1)}X_0$ and $\delta_{total}Y_0$, where E represent location errors in a direction. Thus, Spatial resolutions are $2S$ times normalized spatial resolutions. The normalized vertical resolution distributions are shown in figure 6(a). Our results are the same as those in Hocking's work (Hocking, 2018). The distribution of $\overrightarrow{R_s \delta\theta}$ related, E_2 related and total normalized vertical resolution

distributions are shown in figure 6 from left to right, respectively. In most cases, E_2 is an order of magnitude smaller than $\overrightarrow{R_s\delta\theta}$. Only in the region directly above the receiver does E_2 have the same magnitude as $\overrightarrow{R_s\delta\theta}$. In other words, only in the region directly above the receiver can E_2 influence the total resolution. E_2 is related to the bistatic configuration, but $\overrightarrow{R_s\delta\theta}$ is not. Therefore, in the HM, the distribution of the total vertical resolution is changed slightly varying with **d**. After adding the error term $\overrightarrow{\delta R_t}$, which is related to the bistatic configuration, the normalized total vertical spatial resolution distribution will change visibly varying with **d,** as figure 7's first two rows show. The region between two black lines represents a trustworthy sampling volume for receiver because the elevation angle is beyond $\mathbf{30°}$ with less influence of potential mutual antenna coupling or other obstacles in the surrounding. However, with the transmitter/receiver distance become longer, resolutions in this trustworthy sampling volume are not always acceptable. In figure 7's first row, the transmitter/receiver distance is 300 km and about half of the region between two black line have normalized vertical resolution values lager than 3 km. Because our analytical method can obtain spatial resolutions in 3-dimensional space, figure 7's third row show a perspective to the horizontal section in 90 km altitude for figure 7's second row.

To get an intuitionistic perspective to spatial resolution distribution in 3-dimensional space, figure 8 shows the normalized zonal, meridian and vertical spatial resolution distribution of a multistatic radar link whose transmitter/receiver is 180 km away and the transmitter is south by east $30°$ of the receiver. Classic monostatic meteor radar is a special case of a multistatic meteor radar system whose baseline length is zero. By setting the transmitter/receiver distance to be zero in our program, a monostatic meteor radar's spatial resolution can also be obtained. The spatial resolution distributions are highly symmetrical and correspond to the real characteristics of monostatic meteor radar (not shown in the text, can be seen in the supplement SF1). In the discussion above, the receiver and transmitter antennas are all coplanar. By setting $\psi_x^{X,i}$, $\psi_y^{Y,i}$ and $\psi_z^{Z,i}$ in our program, the non-coplanar receiver/transmitter-antennas situations can also be studied. Slightly tilting of the receiver horizontal plane (for example, set $\psi_x^{X,i}$=$\psi_y^{Y,i} = 5°$) will cause horizontal spatial distributions to change (seen SF2 and SF3 in the supplement). In practical applications, like the Earth's curvature and local topography will lead the receiver horizontal plane tilting. Thus, this kind of tilting should also be taken into account for multistatic meteor radar systems. The details of parameter setting can be seen in the supplement.

The AoAs error propagation process in the receiver has been simplified to eq.(3)-(4) by using the constant PDMEs as the start of error propagation. This is for the sake of the adaptable of our method. If analysing AoAs errors starts from the original voltage signals, the error propagation process will change with a specific receiver interferometer configuration and a specific signal processing method. In practical situations for an unusual receiver antenna configuration or new original signal processing algorithm, an error propagation process based on the specific circumstances needs to be established. Substitute $\delta(\Delta\Psi_1)$ and $\delta(\Delta\Psi_2)$ into other mutually independent measuring errors in a practical situation, and then establishing a new AoAs error propagation to obtain $\delta\theta$ and $\delta\phi$. Or in other words, rewrite the second and third term in eq. (11) to the new established AoAs error propagation matrix and new mutually independent measuring errors respectively. Our analytical method can still work.

It worth noting that except the PDMEs as the start of the error propagation, all the analytical processes are built on the mathematic error propagations. PDMEs include the uncontrolled errors, such as the scattered wave from a few Fresnel zones along meteor trails, phase calibration inaccuracy and noises. However, there are other error sources in practical situation. For example, planes or lightning may make troubles for meteor radar's discrimination system. And interference of obstacles in surroundings will cause further measurement errors of AoAs. These issues are related to actual situations and beyond the scope of this text.

The trustworthy sampling volume is vital for a meteor radar system and it determines the detection area and which meteors could be used in wind retrievals. To avoid the influence of the mutual antenna coupling or the ground clutter, the elevation angle of detection should beyond a threshold, for example $30°$ in general. The spatial resolution is another thing that affects the trustworthy sampling volume. See Figure 7 and SF4 in supplement, only the area of normalized vertical resolution values below 3 km are shown, which represents an acceptable sampling volume. With transmitter/receiver distance increasing, this sampling volume becomes smaller along with the vertical resolution in this volume reduced. This fact limits the transmitter/receiver distance for multistatic meteor radar. Measurement response is important for measuring meteor trails' Doppler shift caused by the background wind. The measured Doppler shift is caused by the component of the wind fields in the Bragg Vector. The smaller the angle between Bragg vector and the wind fields is, the lager this Doppler shift is and meanwhile the higher SNR. The Bragg vector of the multistatic configuration is divergent from the receiver's line of sight. Monostatic meteor radars can only detect winds in radial direction, thus only the mean wind can be solved. By synthesizing monostatic and multistatic the high order component of the wind fields can be solved. The bigger the angle between the Bragg vector and radial direction is, or more diversified Bragg vectors in other words, the more complete and accurate the wind fields will be observed. In short, the trustworthy sampling volume, measurement response and the angular diversity of the Bragg vector should both be taken into account in wind retrievals. The discussion of wind retrievals is beyond the scope of this text and will be in a future work.

4 Conclusion

In this study, we presented the preliminary results of our error analytic method. Our method can calculate the spatial resolution in the zonal, meridian and vertical direction for an arbitrary configuration in three-dimensional space. A detected MTSP can locate within the spatial resolution with equal probability. Higher values of spatial resolution mean that this region needs more meteor counts or averaging to obtain a reliable accuracy. Our method shows that the spatial configuration of a multistatic system will greatly influence the spatial resolution distribution in ENU coordinates and thus will in turn influence the retrieval accuracy of atmospheric parameters such as wind fields. The multistatic meteor radar system's spatial resolution analysis is a key point in analysing the accuracy of retrieved wind and other parameters. The influence of spatial resolutions on wind retrieval will be discussed in the future work. Multistatic radar systems come in many types, and our work in this paper

considers only single-input (single-antenna transmitter) and multi-output (5-antenna interferometric receiver) pulse radar systems. Although single-input multi-output (SIMO) pulse meteor radar is a classic meteor radar system, other meteor radar systems, such as continuous wave radar systems and MISO (multiple-antenna transmitter and single-antenna receiver), show good experimental results and have some advantages over SIMO systems. Using different types of meteor radar systems to constitute the meteor radar network is the future trend and we will add the spatial resolution analyses of other system to the frame of our method in the future. We will validate and apply the error analyses of spatial resolution in horizontal wind determination in a multistatic meteor radar system, which will be built soon in China.

Code availability. The program to calculate the 3D spatial resolution distributions are available in supplement.

Author contributions：W.Z, X.X, W.Y designed the study. W.Z deduced the formulas and wrote the program. W.Z wrote the paper for the first version. X.X supervised the work and provided valuable comments. I.R revised the paper. All of the authors discussed the results and commented on the paper.

Competing interest. The authors declare no conflicts of interests

Acknowledgements. This work is supported by the B-type Strategic Priority Program of CAS Grant No. XDB41000000, the National Natural Science Foundation of China (41774158, 41974174, 41831071 and 41904135), the CNSA pre-research Project on Civil Aerospace Technologies No. D020105, the Fundamental Research Funds for the Central Universities, and the Open Research Project of Large Research Infrastructures of CAS "Study on the interaction between low/mid-latitude atmosphere and ionosphere based on the Chinese Meridian Project." Thanks for Dr.Jia Mingjiao to provide advises and Zeng jie to check equations in this manuscript.

Reference

Browning, K. A., and Wexler, R.: The Determination of Kinematic Properties of a Wind fields Using Doppler Radar, Journal of Applied Meteorology, 7, 105-113, 10.1175/1520-0450(1968)007<0105:Tdokpo>2.0.Co;2, 1968.

Ceplecha, Z., Borovička, J., Elford, W. G., ReVelle, D. O., Hawkes, R. L., Porubčan, V., and Šimek, M.: Meteor Phenomena and Bodies, Space Science Reviews, 84, 327-471, 10.1023/A:1005069928850, 1998.

Chau, J. L., Stober, G., Hall, C. M., Tsutsumi, M., Laskar, F. I., and Hoffmann, P.: Polar mesospheric horizontal divergence and relative vorticity measurements using multiple specular meteor radars, Radio Science, 52, 811-828, 10.1002/2016rs006225, 2017.

Chau, J. L., Urco, J. M., Vierinen, J. P., Volz, R. A., Clahsen, M., Pfeffer, N., and Trautner, J.: Novel specular meteor radar systems using coherent MIMO techniques to study the mesosphere and lower thermosphere, Atmos. Meas. Tech., 12, 2113-2127, 10.5194/amt-12-2113-2019, 2019.

Hocking, W. K., Fuller, B., and Vandepeer, B.: Real-time determination of meteor-related parameters utilizing modem digital technology, Journal of Atmospheric and Solar-Terrestrial Physics, 63, 155-169, 10.1016/s1364-6826(00)00138-3, 2001.

Hocking, W. K.: Spatial distribution of errors associated with multistatic meteor radar, Earth, Planets and Space, 70, 93, 10.1186/s40623-018-0860-2, 2018.

Holdsworth, D. A., Reid, I. M., and Cervera, M. A.: Buckland Park all-sky interferometric meteor radar, Radio Science, 39, 10.1029/2003rs003014, 2004.

Jacobi, C., Hoffmann, P., and K¨¹rschner, D.: Trends in MLT region winds and planetary waves, Collm (52¡ã N, 15¡ã E), Annales Geophysicae (ANGEO), 2008.

Jia, M. J., Xue, X. H., Dou, X. K., Tang, Y. H., Yu, C., Wu, J. F., Xu, J. Y., Yang, G. T., Ning, B. Q., and Hoffmann, L.: A case study of A mesoscale gravity wave in the MLT region using simultaneous multi-instruments in Beijing, Journal of Atmospheric and Solar-Terrestrial Physics, 140, 1-9, 10.1016/j.jastp.2016.01.007, 2016.

Jones, J., Webster, A. R., and Hocking, W. K.: An improved interferometer design for use with meteor radars, Radio Science, 33, 55-65, 10.1029/97rs03050, 1998.

Kang, C.: Meteor radar signal processing and error analysis, 2008.

Philippe, W., and Corbin, H.: On the Analysis of Single-Doppler Radar Data, Journal of Applied Meteorology - J APPL METEOROL, 18, 532-542, 10.1175/1520-0450(1979)018<0532:OTAOSD>2.0.CO;2, 1979.

Reid, I. M.: SOME ASPECTS OF DOPPLER RADAR MEASUREMENTS OF THE MEAN AND FLUCTUATING COMPONENTS OF THE WIND-FIELD IN THE UPPER MIDDLE ATMOSPHERE, Journal of Atmospheric and Terrestrial Physics, 49, 467-484, 10.1016/0021-9169(87)90041-9, 1987.

Spargo, A. J., Reid, I. M., and MacKinnon, A. D.: Multistatic meteor radar observations of gravity-wave–tidal interaction over southern Australia, Atmos. Meas. Tech., 12, 4791-4812, 10.5194/amt-12-4791-2019, 2019.

Stober, G., Sommer, S., Rapp, M., and Latteck, R.: Investigation of gravity waves using horizontally resolved radial velocity measurements, Atmos. Meas. Tech., 6, 2893-2905, 10.5194/amt-6-2893-2013, 2013.

Stober, G., and Chau, J. L.: A multistatic and multifrequency novel approach for specular meteor radars to improve wind measurements in the MLT region, Radio Science, 50, 431-442, 10.1002/2014rs005591, 2015.

Stober, G., Chau, J. L., Vierinen, J., Jacobi, C., and Wilhelm, S.: Retrieving horizontally resolved wind fields using multi-static meteor radar observations, Atmos. Meas. Tech., 11, 4891-4907, 10.5194/amt-11-4891-2018, 2018.

Urco, J. M., Chau, J. L., Weber, T., Vierinen, J. P., and Volz, R.: Sparse Signal Recovery in MIMO Specular Meteor Radars With Waveform Diversity, Ieee Transactions on Geoscience and Remote Sensing, 57, 10088-10098, 10.1109/tgrs.2019.2931375, 2019.

Vaudrin, C. V., Palo, S. E., and Chau, J. L.: Complex Plane Specular Meteor Radar Interferometry, Radio Science, 53, 112-128, 10.1002/2017rs006317, 2018.

Vierinen, J., Chau, J. L., Pfeffer, N., Clahsen, M., and Stober, G.: Coded continuous wave meteor radar, Atmospheric Measurement Techniques, 9, 829-839, 10.5194/amt-9-829-2016, 2016.

Vierinen, J., Chau, J. L., Charuvil, H., Urco, J. M., Clahsen, M., Avsarkisov, V., Marino, R., and Volz, R.: Observing Mesospheric Turbulence With Specular Meteor Radars: A Novel Method for Estimating Second-Order Statistics of Wind Velocity, Earth and Space Science, 6, 1171-1195, 10.1029/2019ea000570, 2019.

Xue, X. H., Dou, X. K., Lei, J., Chen, J. S., Ding, Z. H., Li, T., Gao, Q., Tang, W. W., Cheng, X. W., and Wei, K.: Lower thermospheric-enhanced sodium layers observed at low latitude and possible formation: Case studies, Journal of Geophysical Research-Space Physics, 118, 2409-2418, 10.1002/jgra.50200, 2013.

Yi, W., Xue, X. H., Reid, I. M., Younger, J. P., Chen, J. S., Chen, T. D., and Li, N.: Estimation of Mesospheric Densities at Low Latitudes Using the Kunming Meteor Radar Together With SABER Temperatures, Journal of Geophysical Research-Space Physics, 123, 3183-3195, 10.1002/2017ja025059, 2018.

Younger, J. P., and Reid, I. M.: Interferometer angle-of-arrival determination using precalculated phases, Radio Science, 52, 1058-1066, 10.1002/2017rs006284, 2017.

Appendix

A.1 Coordinates rotation matrix

For a right-handed rectangular coordinate system XYZ, we rotate clockwise Ψ_x about axis-x to obtain a new coordinate. We specify that clockwise rotation satisfies in the right-hand screw rule. A vector in XYZ, denoted as $(x,y,z)^T$, is represented as $(x',y',z')^T$ in the new coordinate. The relationship between $(x,y,z)^T$ and $(x',y',z')^T$ is:

$$\begin{pmatrix} x' \\ y' \\ z' \end{pmatrix} = A_x(\psi_x)\begin{pmatrix} x \\ y \\ z \end{pmatrix} = \begin{pmatrix} 1 & 0 & 0 \\ 0 & cos\psi_x & sin\psi_x \\ 0 & -sin\psi_x & cos\psi_x \end{pmatrix}\begin{pmatrix} x \\ y \\ z \end{pmatrix} \quad \text{(A1.1)}$$

Similarly, we rotate clockwise Ψ_y ~~is~~ about axis-y to obtain a new coordinate. The presentation for a vector in new coordinates and original can be linked by a matrix, $A_y(\psi_y)$:

$$A_y(\psi_y) = \begin{pmatrix} cos\psi_y & 0 & -sin\psi_y \\ 0 & 1 & 0 \\ sin\psi_y & 0 & cos\psi_y \end{pmatrix} \quad \text{(A1.2)}$$

we rotate clockwise Ψ_z about axis-z to obtain a new coordinate. The presentation for a vector in new coordinates and original can be linked by a matrix $A_z(\psi_z)$:

$$A_z(\psi_z) = \begin{pmatrix} cos\psi_z & sin\psi_z & 0 \\ -sin\psi_z & cos\psi_z & 0 \\ 0 & 0 & 1 \end{pmatrix} \quad \text{(A1.3)}$$

For any two coordinate systems XYZ and $X'Y'Z'$ with co-origin, one can always rotate clockwise Ψ_x, Ψ_y and ψ_z in order of axis-X, Y, Z respectively, transforming XYZ to $X'Y'Z'$ (figure A.1). The presentation for a vector in $X'Y'Z'$ and XYZ can be linked by a matrix, $A_R(\psi_x, \psi_y, \psi_z)$:

$$A_R(\psi_x, \psi_y, \psi_z) = A_z(\psi_z)A_y(\psi_y)A_x(\psi_x) = \begin{pmatrix} cos\psi_y cos\psi_z & sin\psi_x sin\psi_y cos\psi_z + cos\psi_x sin\psi_z & -cos\psi_x sin\psi_y cos\psi_z + sin\psi_x sin\psi_z \\ -cos\psi_y sin\psi_z & -sin\psi_x sin\psi_y sin\psi_z + cos\psi_x cos\psi_z & cos\psi_x sin\psi_y sin\psi_z + sin\psi_x cos\psi_z \\ sin\psi_y & -sin\psi_x cos\psi_y & cos\,\psi_x cos\psi_y \end{pmatrix} \quad \text{(A1.4)}$$

We call $A_R(\psi_x, \psi_y, \psi_z)$ as the coordinates rotation matrix.

A.2 AoAs measuring errors

In coordinate XYZ, AoAs includes zenith angle θ and azimuth angle ϕ. In the plane wave approximation, the radio wave is at angle γ_1 and γ_2 with an antenna array (figure A.2). There is a phase difference $\Delta\Psi_1$ and $\Delta\Psi_2$ between two antennas (figure 1). See figure 1, $\Delta\Psi_1$ and $\Delta\Psi_2$ can be expressed as:

$$\Delta\Psi_1 = \frac{2\pi D_1 cos\gamma_1}{\lambda} \quad \text{(A2.1)}$$

$$\Delta\Psi_2 = \frac{2\pi D_2 cos\gamma_2}{\lambda} \quad \text{(A2.2)}$$

Using γ_1, γ_2 the AoAs can be expressed as:

$$\cos^2\gamma_1 + \cos^2\gamma_2 + \cos^2\theta = 1 \quad \text{(A2.3)}$$

$$tan\phi = \frac{cos\gamma_2}{cos\gamma_1} \quad \text{(A2.4)}$$

Or in another expression:

$$\cos\gamma_1 = \sin\theta\cos\phi \quad \text{(A2.5)}$$

$$\cos\gamma_2 = \sin\theta\sin\phi \quad \text{(A2.6)}$$

substitute $cos\gamma_1$ and $cos\gamma_2$ in (A2.3) and (A2.4) by using (A2.1) and (A2.2):

$$\cos^2\theta = 1 - \left(\frac{\lambda}{2\pi}\right)^2 \left(\frac{\Delta^2\Psi_1}{D_1^2} + \frac{\Delta^2\Psi_2}{D_2^2}\right) \quad \text{(A2.7)}$$

$$\ln(\tan\phi) = \ln(D_1\Delta\Psi_2) - \ln(D_2\Delta\Psi_1) \quad \text{(A2.8)}$$

(A2.7) and (A2.8) link the phase difference with the AoAs and expanding θ and ϕ, $\Delta\Psi_1$ and $\Delta\Psi_2$ to first order:

$$2cos\theta sin\theta\delta\theta = \left(\frac{\lambda}{2\pi}\right)^2 \left[\frac{2\Delta\Psi_1\delta(\Delta\Psi_1)}{D_1^2} + \frac{2\Delta\Psi_2\delta(\Delta\Psi_2)}{D_2^2}\right] \quad \text{(A2.9)}$$

$$\delta\phi = \frac{sin\phi cos\phi}{\Delta\Psi_2}\delta(\Delta\Psi_2) - \frac{sin\phi cos\phi}{\Delta\Psi_1}\delta(\Delta\Psi_1) \quad \text{(A2.10)}$$

For (A2.9) and (A2.10), substitute $\Delta\Psi_1$ and $\Delta\Psi_2$ using (A2.1), (A2.2) and (A2.5), (A2.6) to the functions of θ, ϕ. Now, eq. (3) and eq. (4) have been proven. If the zenith angle $\theta = 0°$, we stipulate that $\frac{\cos\phi}{\sin\theta}$ and $\frac{\sin\phi}{\sin\theta}$ are 1.

A.3 Radial distance measuring error

Expand R_s, R and $cos\alpha$ in eq.(1) to first order, δR_s can be expressed as a function of δR and $\delta(\cos\alpha)$:

$$\delta R_s = \frac{R^2 - 2Rd\cos\alpha + d^2}{2(R - d\cos\alpha)^2}\,\delta R + \frac{d(R^2 - d^2)}{2(R - d\cos\alpha)^2}\,\delta(\cos\alpha) \quad \text{(A3.1)}$$

α is the angle between R_s and axis-X_i. We denote the zenith and azimuth angles in coordinate-$X_iY_iZ_i$ as θ' and ϕ', respectively. And the relationship between α and θ', ϕ' is

$$cos\alpha = sin\theta' cos\phi' \quad \text{(A3.2)}$$

Using coordinates rotation matrix $A_R(\psi_x^{X,i}, \psi_y^{Y,i}, \psi_z^{Z,i})$, $sin\theta' cos\phi'$ can be expressed as the function of AoAs:

$$\sin\theta'\cos\phi' = A_{11}\sin\theta\cos\phi + A_{12}\sin\theta\sin\phi + A_{13}\cos\theta \quad \text{(A3.3)}$$

A_{ij} are represent the elements in matrix $A_R(\psi_x^{X,i}, \psi_y^{Y,i}, \psi_z^{Z,i})$ for $i, j = 1,2,3$.

Using (A3.2) and (A3.3), $\delta(\cos\alpha)$ can be expressed as a function of $\delta\theta$ and $\delta\phi$ as:

$$\delta(\cos\alpha) = (A_{11}\cos\theta\cos\phi + A_{12}\cos\theta\sin\phi - A_{13}\sin\theta)\delta\theta + (-A_{11}\sin\theta\sin\phi + A_{12}\sin\theta\cos\phi)\delta\phi \quad \text{(A3.4)}$$

Finally, δR_s can be expressed as the function of $\delta R, \delta\theta, \delta\phi$ as:

$$\delta R_s = F(\delta R, \delta\theta, \delta\phi) = f_R(\theta,\phi)\delta R + f_\theta(\theta,\phi)\delta\theta + f_\phi(\theta,\phi)\delta\phi \quad \text{(A3.5)}$$

For:

$$f_R(\theta,\phi) = \frac{d^2 + R^2 - 2Rd(A_{11}\sin\theta cos\phi + A_{12}sin\theta sin\phi + A_{13}cos\theta)}{2[R - d(A_{11}\sin\theta cos\phi + A_{12}sin\theta sin\phi + A_{13}cos\theta)]^2} \quad \text{(A3.6)}$$

$$f_\theta(\theta,\phi)=\frac{d(R^2-d^2)(\boldsymbol{A_{11}cos\theta cos\phi+A_{12}cos\theta sin\phi-A_{13}sin\theta})}{2[R-d(\mathrm{A}_{11}\sin\theta cos\phi+A_{12}sin\theta sin\phi+A_{13}cos\theta)]^2}$$

(A3.7)

$$f_\phi(\theta,\phi)=\frac{d(R^2-d^2)(\boldsymbol{-A_{11}sin\theta sin\phi+A_{12}sin\theta cos\phi})}{2[R-d(\mathrm{A}_{11}\sin\theta cos\phi+A_{12}sin\theta sin\phi+A_{13}cos\theta)]^2}$$

(A3.8)

A.4 True error of E_2

See figure 4 (b), the total length of side AC and side AB represents the pulse width. Side AC equals side CB and they both equal to half of the pulse S. In $X_iY_iZ_i$, the presentation of point A is $(\mathrm{x_i},\mathrm{y_i},\mathrm{z_i})$, the receiver is (0,0,0) and T_i is (d,0,0). The distance between T_i and A is $R_i=R-R_s$. We denote that the presentation of point B and C in $X_iY_iZ_i$ is (x_B,y_B,z_B) and (x_C,y_C,z_C), respectively. We use vector collinear to establish equations for B and C. Therefore, one can obtain the coordinates of point B and C by the following equations:

$$(x_B,y_B,z_B)^T=\frac{R_s-S}{R_s}\ (x_\mathrm{i},y_\mathrm{i},z_\mathrm{i})^T \tag{A4.1}$$

$$(x_C-d,y_C,z_C)^T=\frac{R_\mathrm{i}-S}{R_\mathrm{i}}\ (x_\mathrm{i}-d,y_\mathrm{i},z_\mathrm{i})^T \tag{A4.2}$$

For isosceles triangle ABC, the perpendicular line AD intersects side CB in middle point D. Then, we obtain the coordinate value of D in $X_iY_iZ_i$ as:

$$(\mathrm{x_D},\mathrm{y_D},\mathrm{z_D})=\frac{1}{2}(\mathrm{x_B}+\mathrm{x_c},\mathrm{y_B}+\mathrm{y_c},\mathrm{z_b}+\mathrm{z_c})=\frac{1}{2}((a_1+a_2)\mathrm{x_i}-a_2\mathrm{d}+\mathrm{d},(a_1+a_2)\mathrm{y_i},(a_1+a_2)\mathrm{z_i}) \tag{A4.3}$$

We denote $a_1=\frac{R_s-S}{R_s}$, $a_2=\frac{R_i-S}{R_i}$. Finally, one can obtain the error vector of E_2 as vector $\overrightarrow{DA}$ in $X_iY_iZ_i$:

$$\boldsymbol{\overrightarrow{DA}}=\left(\frac{(2-a_1-a_2)x_\mathrm{i}+d(a_2-1)}{2},\ \frac{2-a_1-a_2}{2}\boldsymbol{y_\mathrm{i}},\frac{2-a_1-a_2}{2}\boldsymbol{z_\mathrm{i}}\right)^{\boldsymbol{T}} \tag{A4.4}$$

A.5 calculate AoAs and range information in $X_iY_iZ_i$

For a space point $(\mathrm{x_i},\mathrm{y_i},\mathrm{z_i})$ in $X_iY_iZ_i$ which represent a MTSP, $\mathrm{R_s}$ can be solved easily as:

$$\overrightarrow{\mathrm{R_s}}=(\mathrm{x_i},\mathrm{y_i},\mathrm{z_i})$$

$$\mathrm{R_s}=\sqrt{x_i^2+y_i^2+z_i^2} \tag{A6.1}$$

The distance between transmitter $\mathrm{T_i}$ and receiver $\mathrm{R_X}$ is $\mathrm{d_i}$ as sketched in figure 4(a). Thus, coordinate value of $\mathrm{T_i}$ in $X_iY_iZ_i$ is $(\mathrm{d_i},0,0)$ and $\mathrm{R_i}$ can be solved as:

$$R_i = \sqrt{(x_i - d_i)^2 + y_i^2 + z_i^2} \quad \text{(A6.2)}$$

Before we calculate AoAs in $X_iY_iZ_i$, the representation of unit vectors of axis-X, Y, Z in $X_iY_iZ_i$ need to know. In XYZ those unit vectors are easily represented as $(1,0,0)^T$, $(0,1,0)^T$, $(0,0,1)^T$. Though coordinates rotation matrix $A_R(\psi_x^{X,i}, \psi_y^{Y,i}, \psi_z^{Z,i})$, one can get those unit vector's representation in $X_iY_iZ_i$ as:

$$\overrightarrow{n_x} = (A_{11}, A_{21}, A_{31})^T$$
$$\overrightarrow{n_y} = (A_{12}, A_{22}, A_{32})^T$$
$$\overrightarrow{n_z} = (A_{13}, A_{23}, A_{33})^T \quad \text{(A6.3)}$$

For $\overrightarrow{n_x}$, $\overrightarrow{n_y}$ and $\overrightarrow{n_z}$ are unit vectors of Axis-X, Y, Z respectively. And A_{ij} are the elements in 3×3 matrix $A_R(\psi_x^{X,i}, \psi_y^{Y,i}, \psi_z^{Z,i})$ for $i, j = 1,2,3$. Now AoAs can get as:

$$\cos\theta = \frac{\overrightarrow{R_s}}{R_s} \cdot \overrightarrow{n_z} \quad \text{(A6.4)}$$

$$\sin\theta = \sqrt{1 - \cos^2\theta}$$

(A6.5)

$$\cos\phi = \frac{\overrightarrow{R_s}}{R_s} \cdot \frac{\overrightarrow{n_x}}{\sin\theta}$$

(A6.6)

$$\sin\phi = \frac{\overrightarrow{R_s}}{R_s} \cdot \frac{\overrightarrow{n_y}}{\sin\theta} \quad \text{(A6.7)}$$

For $0° < \theta < 180°$ and $0° \leq \phi < 360°$. When $\theta = 0°$, we handle it as same as in **Appendix (A.2)**.

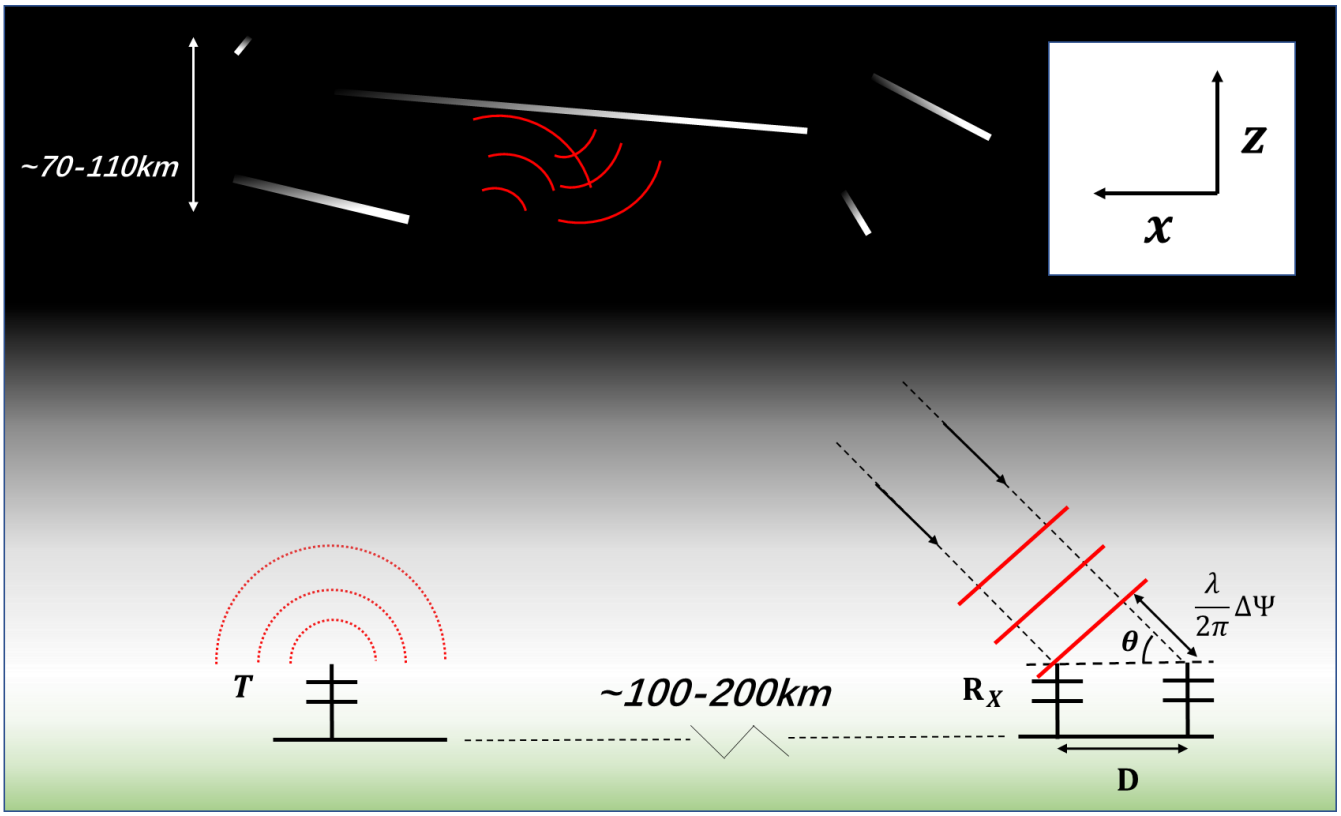

Figure 1：Schematic diagram of a simplified bistatic configuration used in Hocking's vertical resolution analysis(Hocking, 2018). The two receiver antennas and a transmitter antenna are collinear. The analysis is in a 2-dimensional vertical section through the baseline. The radio wave is scattered by a few Fresnel zones of several kilometres long around specular point in meteor trail and received by receiver antennas. The cross-correlation analysis between receiver antennas can solve the AoAs. The fact that the radio wave bounced back from a few Fennel zones will cause the measured phase difference between the receiver antenna pair deviating from the ideal phase difference. The ideal phase difference will solve an AoAs pointing to MTSP. This deviation from the ideal phase difference is one of the error sources of PDME.

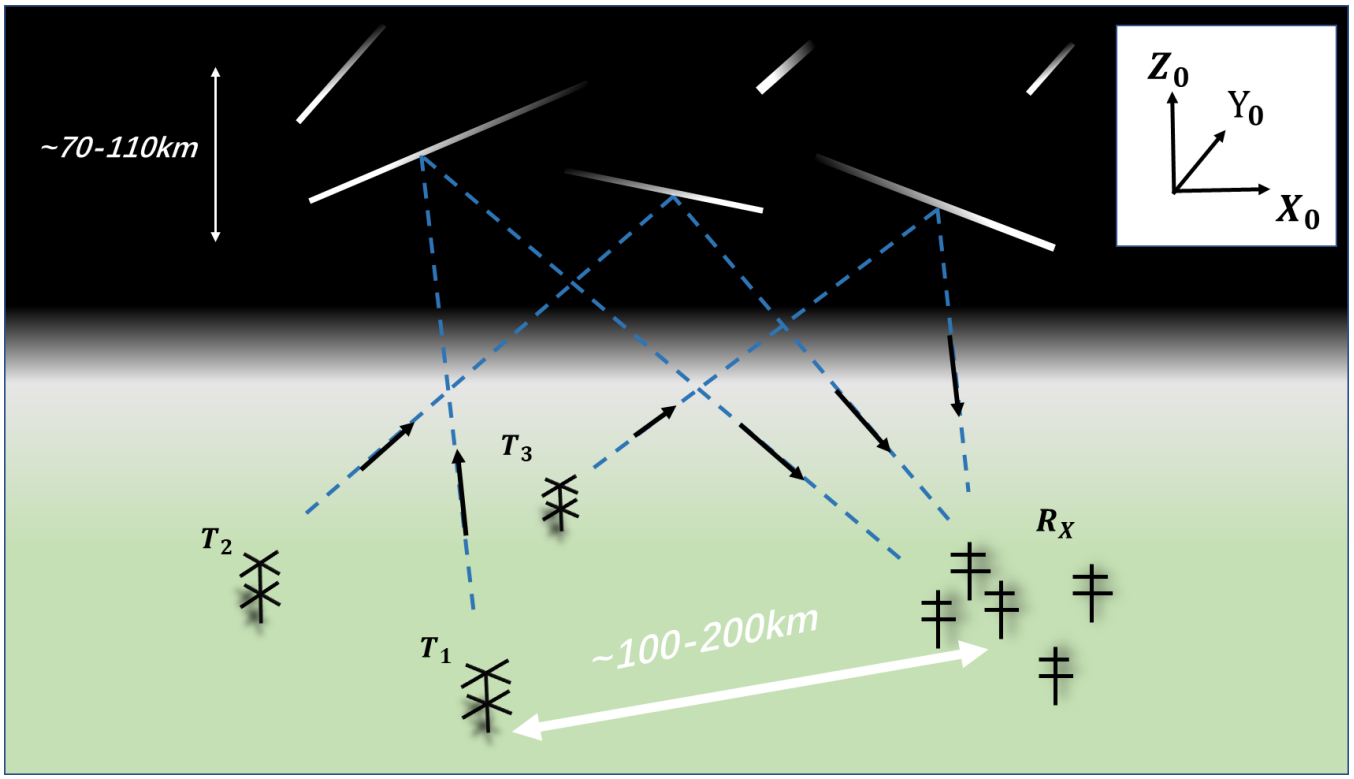

Figure 2: Schematic diagram of a multistatic meteor radar system using SIMO (single-input and multi-output). There are three transmitters (T_1, T_2 and T_3) and one receiver (R_X) in the picture. The transmitter/receiver distance is usually approximately 100-200 km. X_0, Y_0, Z_0 represents the east, north and up directions of the receiver. Over 90% of the received energy comes from about one kilometre around specular point of the meteor trail, which is slightly less than the length of the central Fresnel zone (Ceplecha et al., 1998).

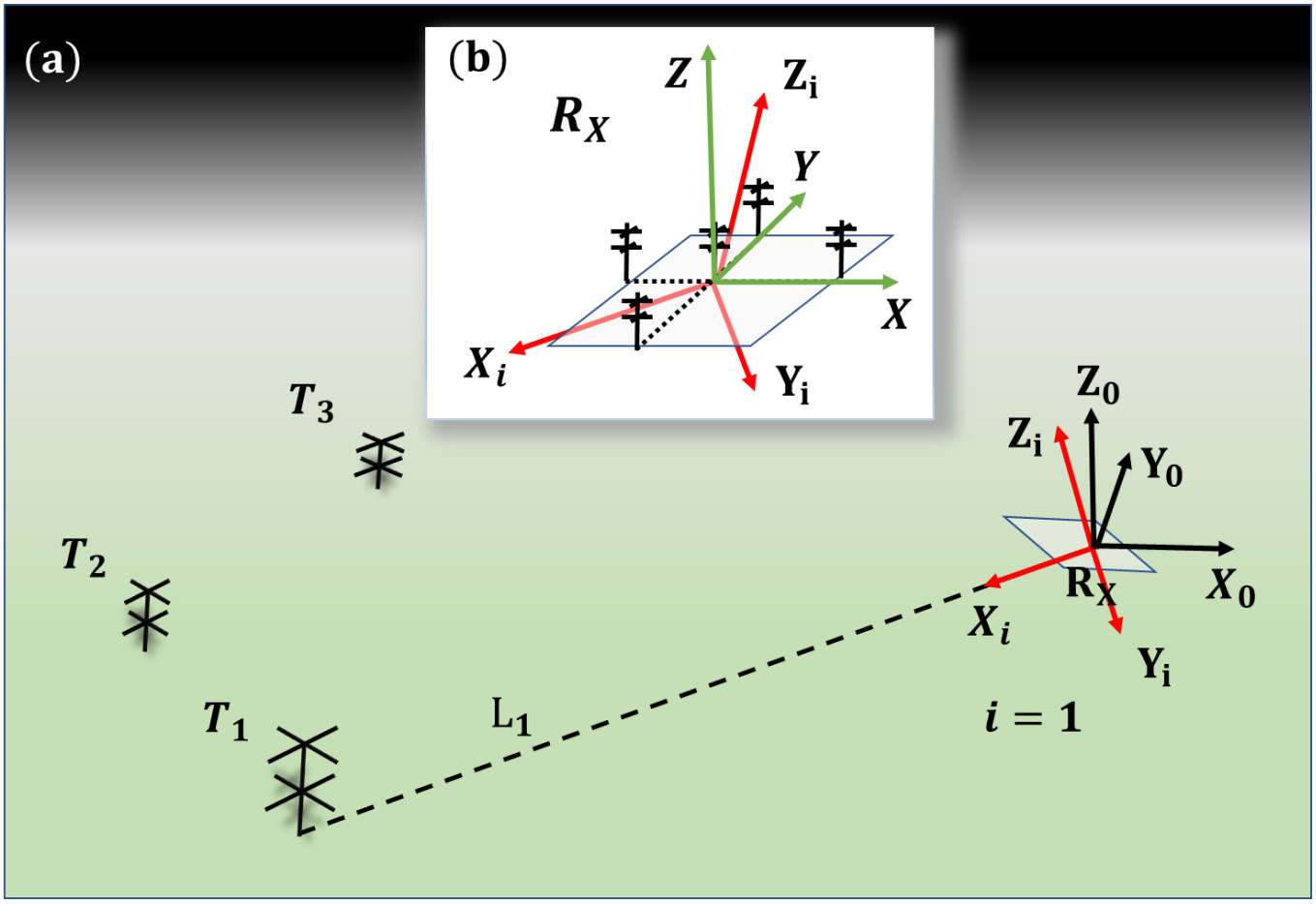

Figure 3: (a) Schematic diagram of the three introduced coordinate systems. $X_iY_iZ_i$ are a class of coordinate systems whose axis-X_i point to transmitter i. And in this picture, i are 1,2,3. $X_0Y_0Z_0$ is the ENU coordinate system and all errors will be compared in this coordinate. (b) Magnified plot of the receiver. XYZ is fixed on the receiver horizontal plane. Axis-X and Y are collinear to two antenna arrays.

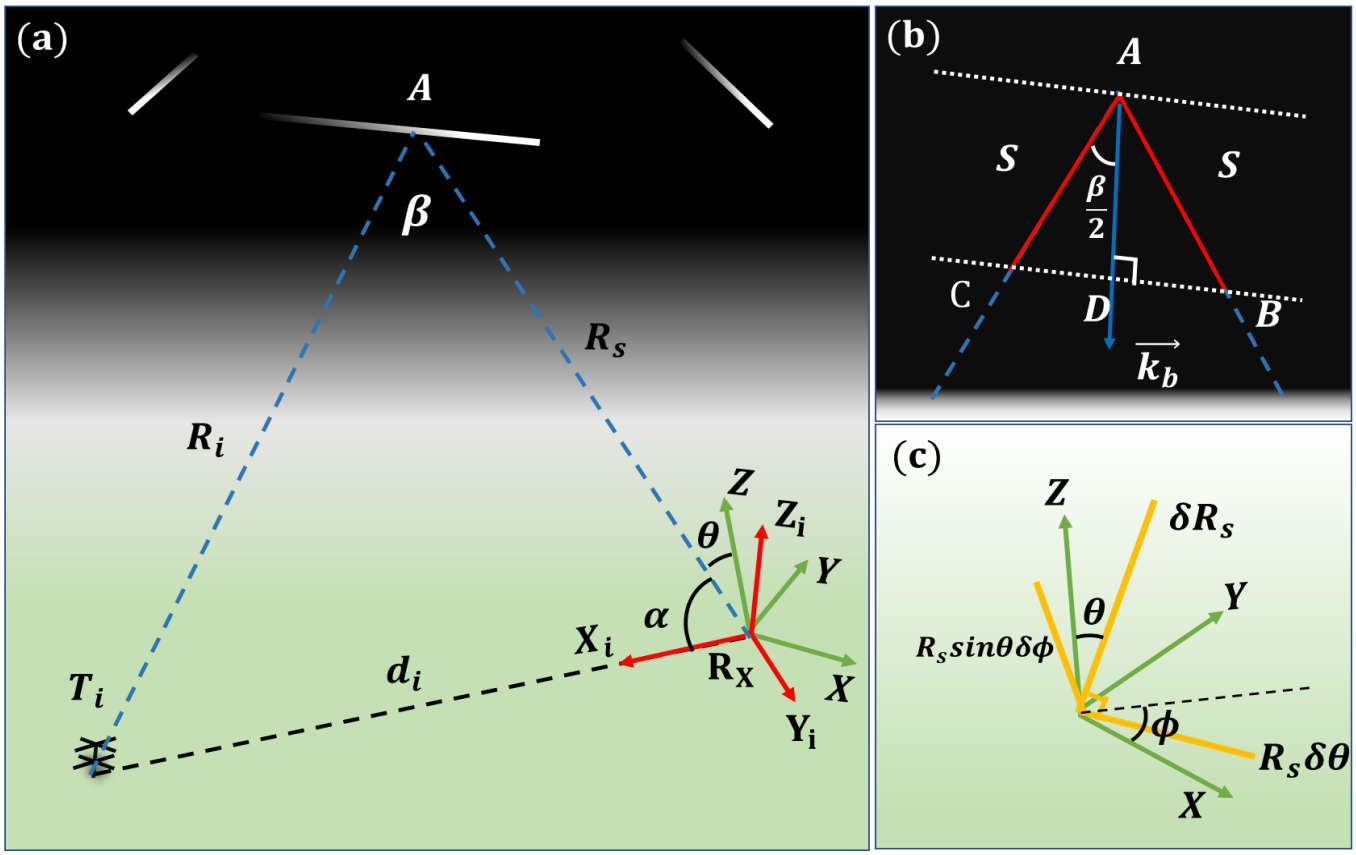

Figure 4: (a) Schematic diagram of a forward scatter geometry for the radar link between T_i and R_X. Point-A is the MTSP. (b) Magnified plot of specular point A. The red line represents a radio wave pulse, and S is the half wave pulse length. $\overrightarrow{k_b}$ is the Bragg vector which halves forward scatter angle β. (c) Schematic diagram of E_1 in XYZ, which can be decomposed into three orthogonal vectors.

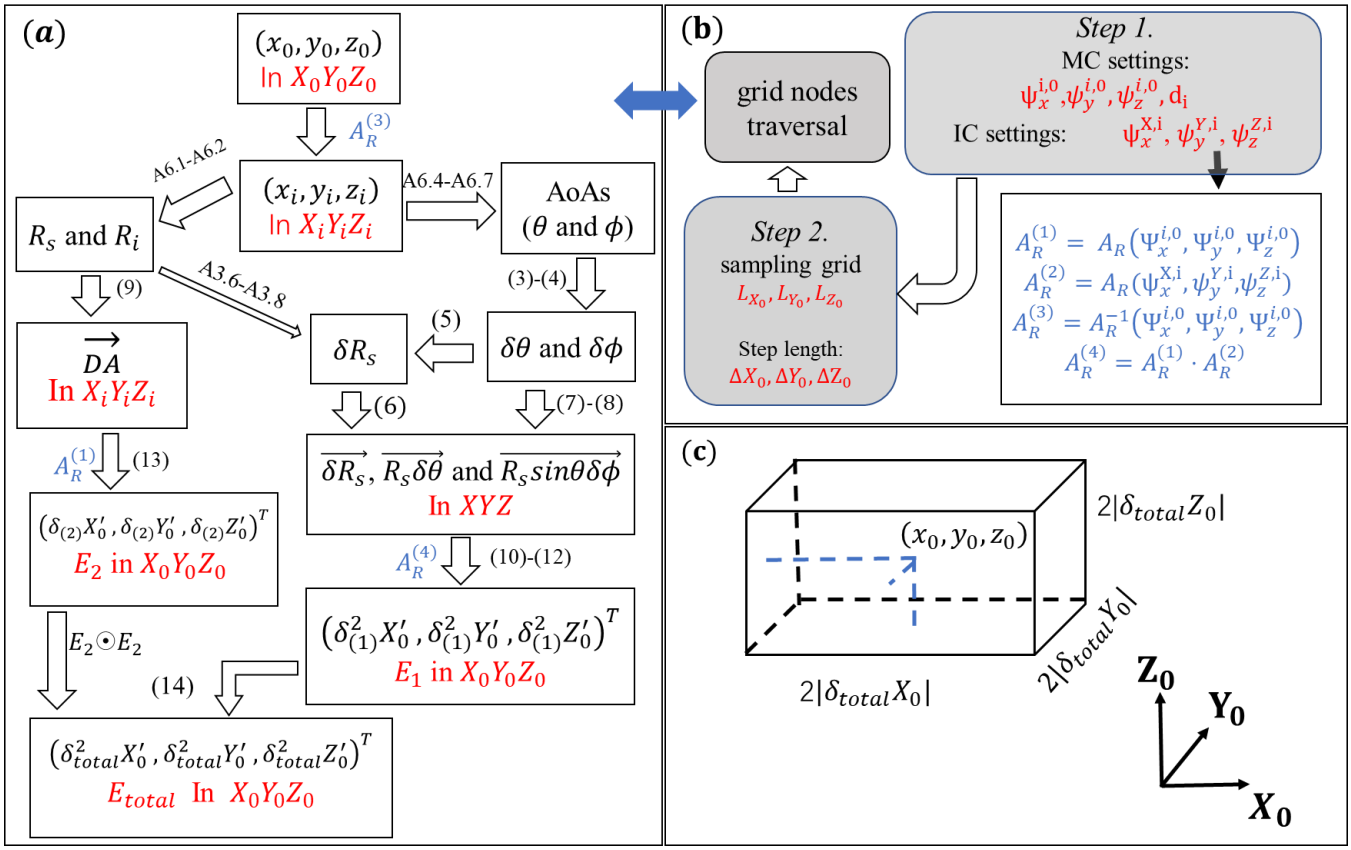

Figure 5: (a) the flow chart of the location error calculation process for a point in $X_0Y_0Z_0$. The marks beside arrows represent the corresponding equations (black) or coordinate rotation matrix (blue) in the paper. "⊙" is the Hadamard product. Thus $E_2 \odot E_2$ will get $(\delta_{(2)}^2X_0, \delta_{(2)}^2Y_0, \delta_{(2)}^2Z_0)^T$. (b) the flow chart of the program to calculate the location errors distributions for a radar link L_i. This process includes parameters settings for a radar link, generating sampling grid nodes and traversing all the nodes. For each node, the program uses the calculation method described in (a). MC: multistatic configuration, IC: interferometer (receiver antennas) configuration. (c) Schematic diagram of relationship between the spatial resolution and the total location errors of the MTSP. For a detected point in space, the MSE of MTSP's location errors is $\pm|\delta_{total}X_0|$, $\pm|\delta_{total}Y_0|$, $\pm|\delta_{total}Z_0|$ in zonal, meridian and vertical respectively. This means that the actual specular point might occur in a region which form a $2|\delta_{total}X_0| \times 2|\delta_{total}Y_0| \times 2|\delta_{total}Z_0|$ cube and the detected point is on the central of this cube.

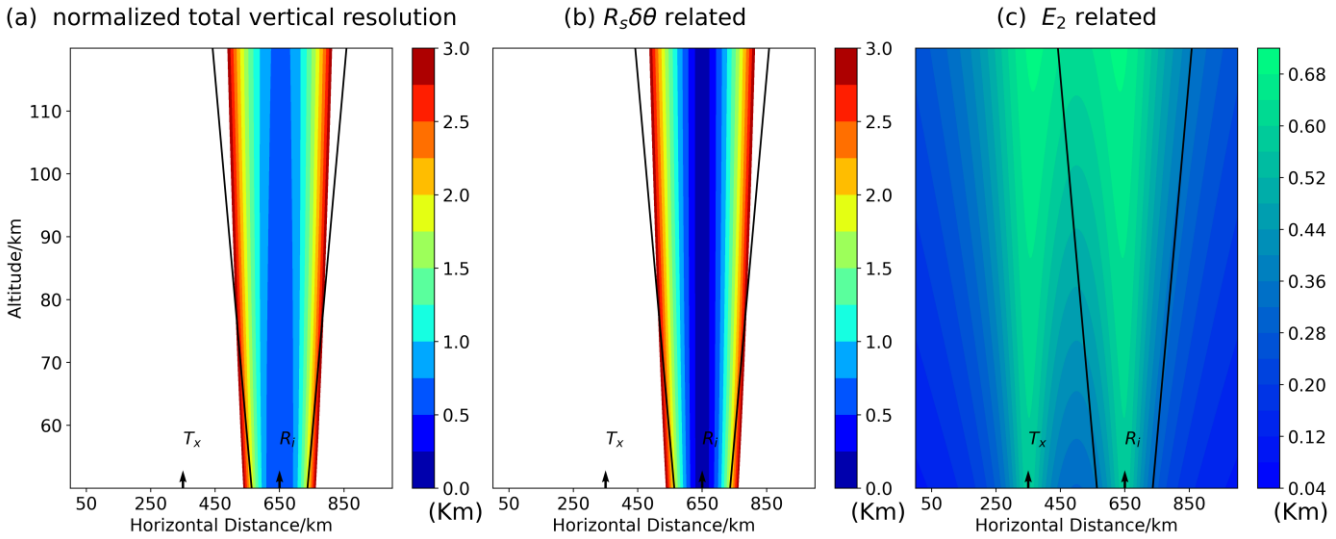

Figure 6: the normalized vertical resolution distribution in a vertical section from 50 km to 60 km height when ignore the error term "δR_s". (a), (b), (c) are total, $R_s\delta\theta$ related and E_2 related normalized resolution distribution respectively. The results is ~~the~~as same as Hocking's work (Hocking, 2018). Two black arrows represent the positions right above transmitter and receiver and transmitter/receiver are 300 km away. The region between two black oblique lines is ~~a~~ the trustworthy sampling volume for the receiver because the elevation angle is beyond $30°$ with little influence ~~of~~ from potential mutual antenna coupling or other obstacles in the surrounding. Except the region in large elevation angle (i.e. $90°$), E_2 related resolution values are much lower than $R_s\delta\theta$ related. $R_s\delta\theta$ related resolution distribution is only depend on the receiver. Thus, the total vertical resolution distribution is nearly unchanged with transmitter/receiver distance varying. The normalized resolution values exceed 3 km which correspond 12 km vertical resolution aren't shown.

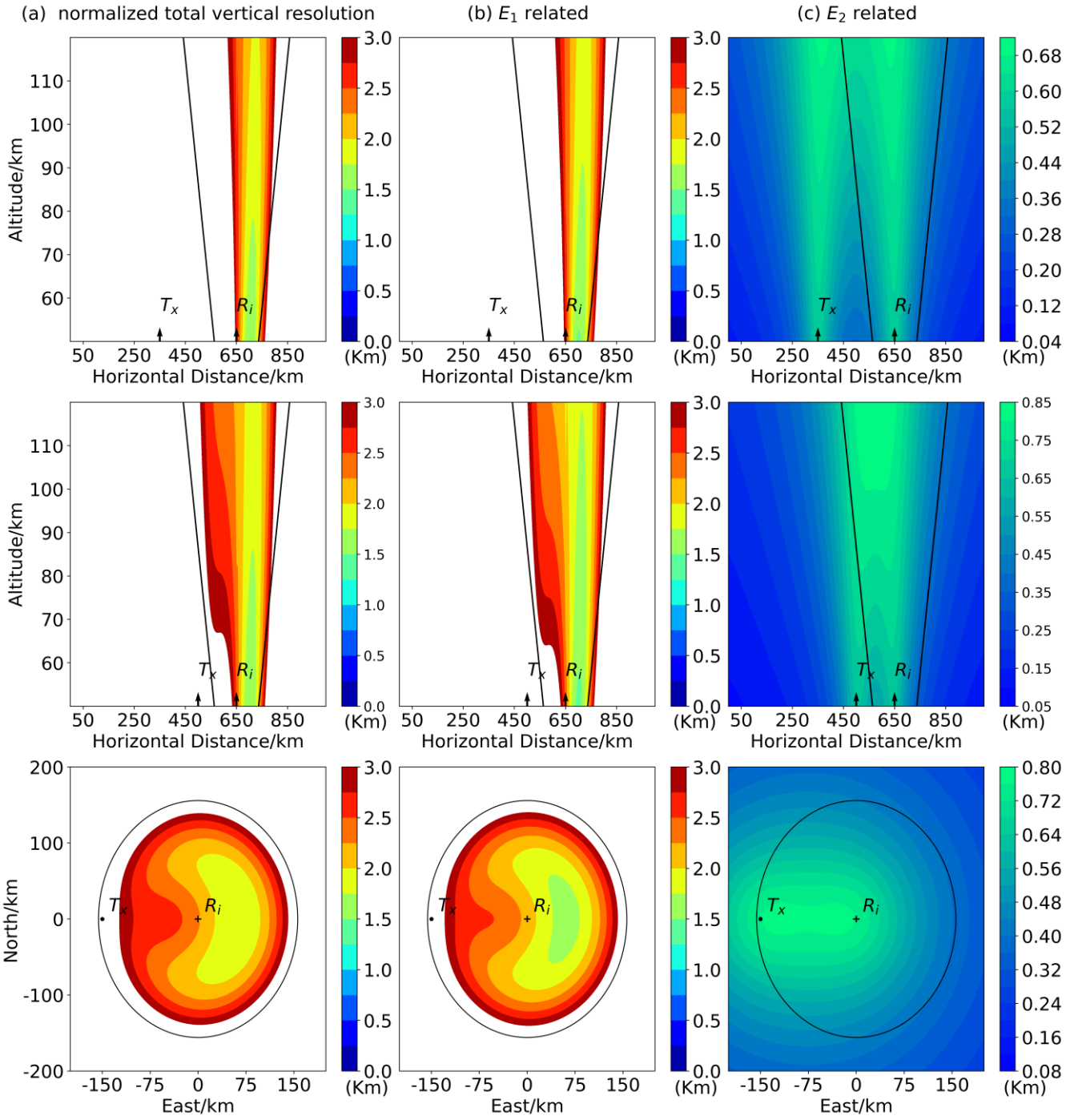

Figure 7：the normalized vertical resolution distribution using the analytical method in this paper. The first and second row represent a vertical section from height 50 km to 120 km. The third row represent the horizontal section in 90 km and the receiver is on the origin with positive coordinate value represent east or north direction. The first row has the same parameters settings as Figure 6 and is used to compare with Figure 6. E_1 related resolution will change with transmitter/receiver configuration because it consider the error term "δR_s". Thus, the total vertical resolution will change with transmitter/receiver configuration. With

transmitter/receiver distance varying from 300 km (the first row) to 150 km (the second row), the total vertical resolution distribution is changed. The third row is the perspective to the horizontal section in 90 km altitude for the second row. The normalized resolution values exceed 3 km aren't shown.

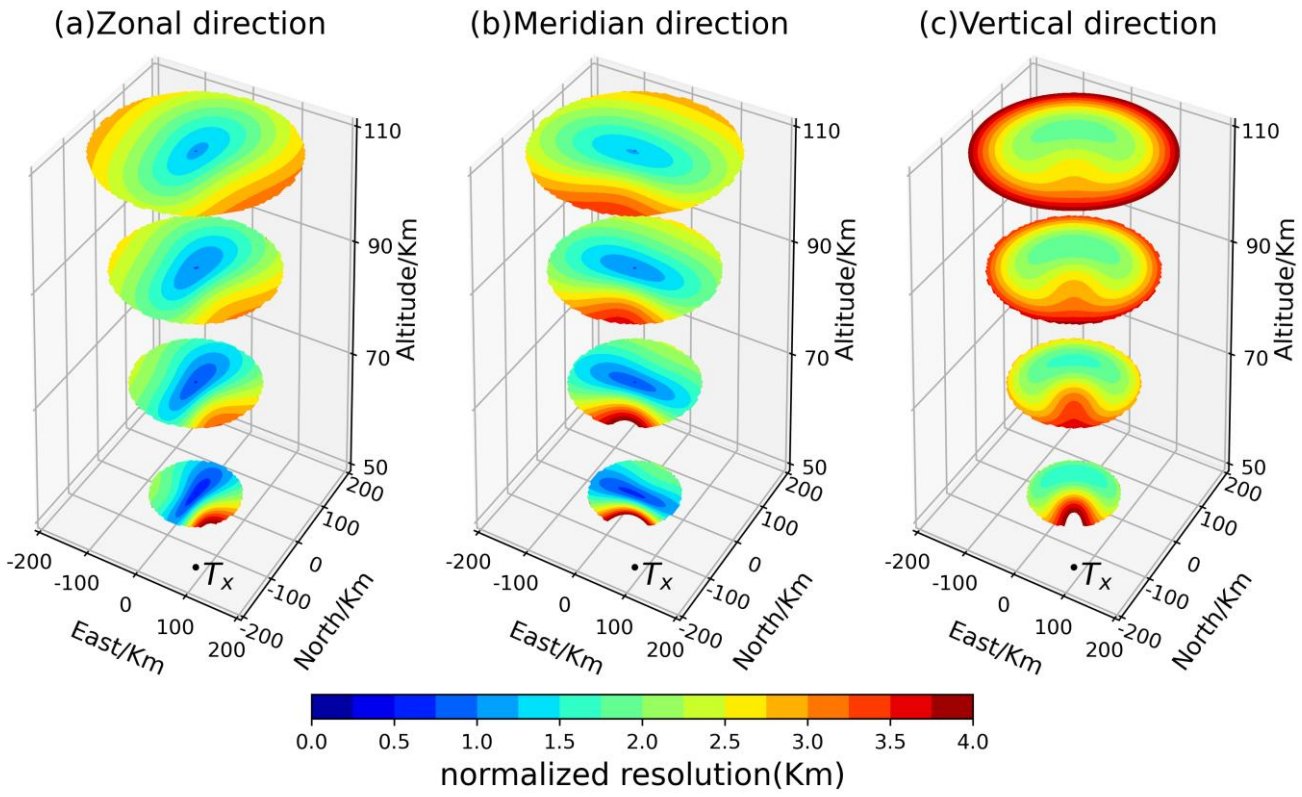

Figure 8 the 3D contourf plot of normalized resolution distribution for a multistatic radar link whose baseline length is 180 km and transmitter is south by east 30° of the receiver. The black dots represent the position right above transmitter and the receiver is on the origin of axes. (a), (b) and (c) are the normalized resolution distribution in zonal, meridian and vertical respectively. The subplot's four slice circle from bottom to top are the horizontal section in 50 km, 70 km, 90 km and 110 km height. The region whose elevation angle of the receiver is less than 30° isn't shown and therefore the slice circles become larger from the bottom to the top. The normalized resolution values exceed 4 km which correspond 16 km resolution aren't shown.

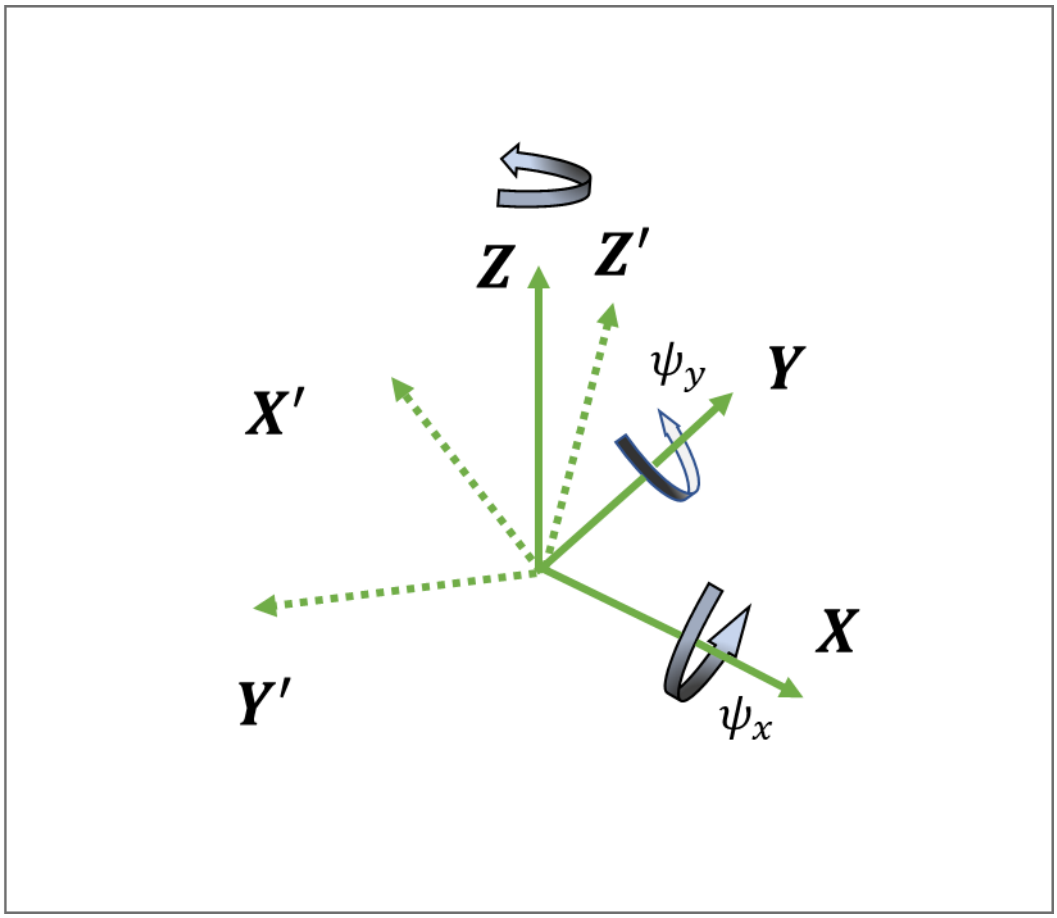

Figure A.1

630

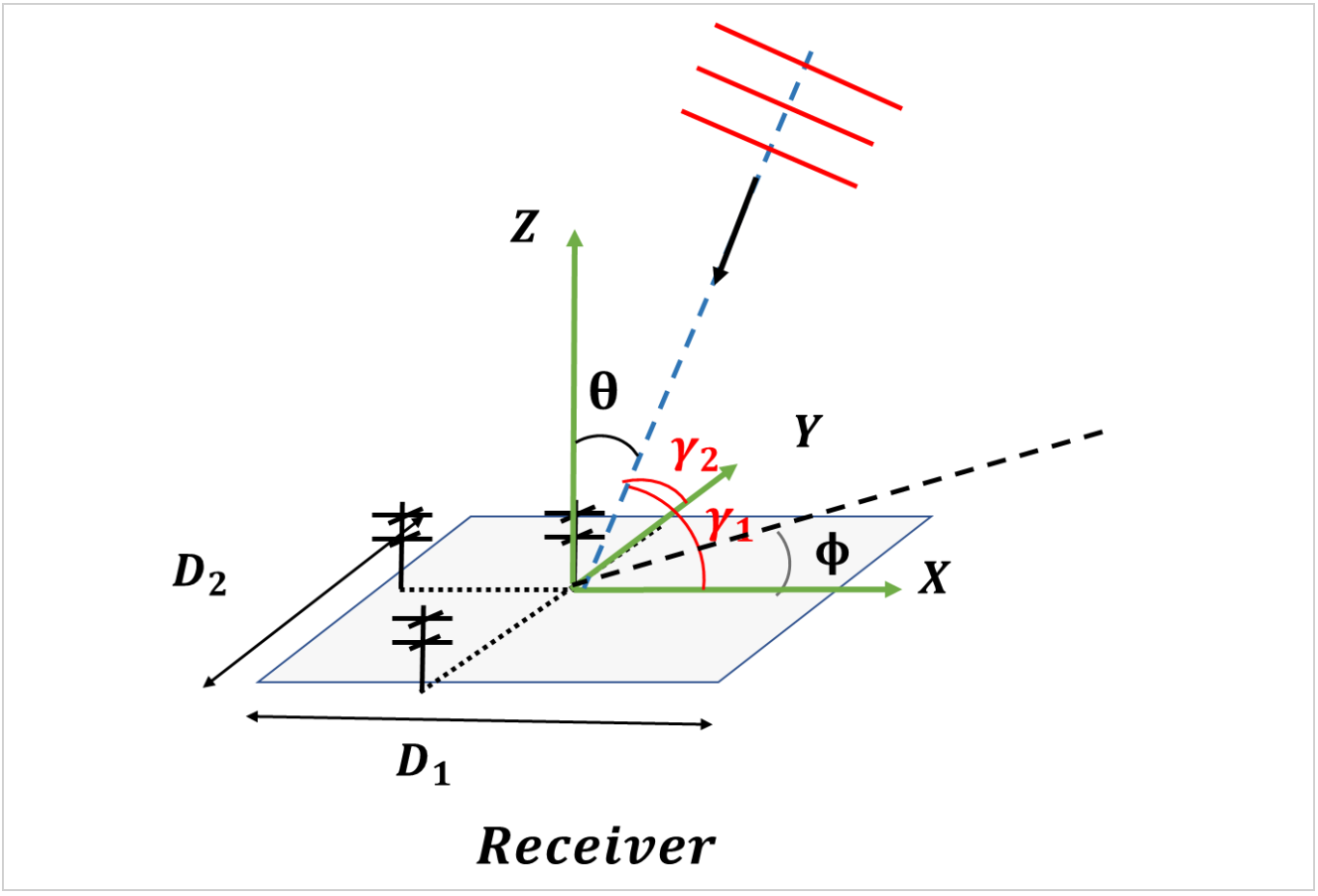

Figure A.2 (two antennas are not shown for concise)